Chiang *et al. Earth, Planets and Space* (2022) 74:39
https://doi.org/10.1186/s40623-022-01596-4

Earth, Planets and Space

FULL PAPER

Enhancement of equatorial OI(1D) emissions at midnight

Chih-Yu Chiang, Tzu-Fang Chang* and Sunny W. Y. Tam

Abstract

A number of recent studies have highlighted observational evidence of midnight brightness of the 630.0 nm nightglow, which is usually related to the midnight temperature maximum (MTM) effect. In this report, MTM-related enhancements of the 630.0 nm airglow around midnight are observed through images from the ISUAL/FORMOSAT-2 satellite. The data statistics are classified into three specific types (no-peak, single-peaked, and double-peaked events) and separated into the different seasons. In order to understand the influences of geomagnetic conditions, the statistical analyses are also separated into two regions. One is collected from the region whose geomagnetic equator is north of the geographic equator, and the other is collected from the region whose geomagnetic equator is south of the geographic equator. The results show that the single-peaked brightness often appears between the geographic equator and the geomagnetic equator. The double-peaked brightness appears simultaneously on the two sides of the region sandwiched by the two equators. Coupled with the summer-to-winter neutral wind generated by seasonal effects, one side of brightness could be enhanced or disappear due to the plasma moving along the field line. The no-peak events mainly occur close to May–July, which may be due to the effect of ionospheric annual anomalies. Overall, the statistical results for the occurrence rate show strong seasonal variations with different cycles at different longitudinal regions for all three types of events.

Keywords: Midnight temperature maximum, ISUAL, 630.0 nm, SAMI-2, Airglow

*Correspondence: jocelyn@pssc.ncku.edu.tw
Institute of Space and Plasma Sciences, National Cheng Kung University, Tainan 70101, Taiwan

Graphical Abstract

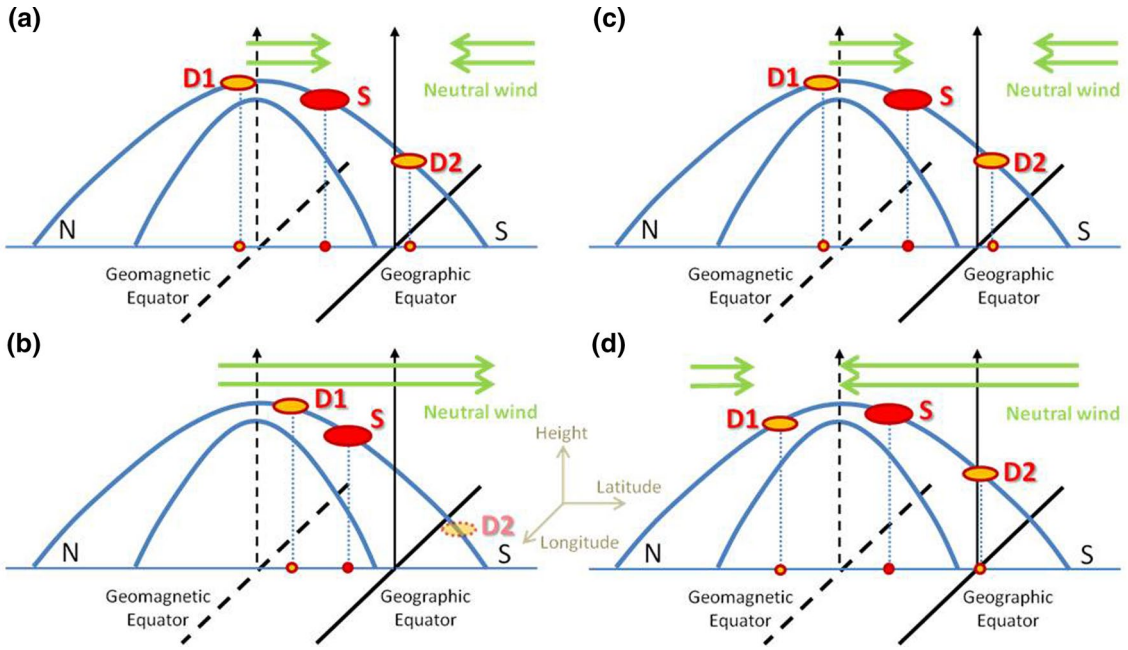

Introduction

The enhancement of the OI(^{1}D) airglow at the characteristic spectral line of 630.0 nm is typically observed at equatorial latitudes at midnight. The volume emission rate of the 630.0 nm nightglow in the F2 region (Sobral et al. 1993) can be expressed as follows:

$$I_{630} = \frac{A_{1D}\mu_D\gamma[O_2]\left[O^+\right]}{k_1[N_2] + k_2[O_2] + k_3[O] + A_{1D} + A_{2D}}, \quad (1)$$

where μ_D is the quantum yield of O(^{1}D); γ is the rate coefficient of the charge exchange process between O^+ and O_2; k_1, k_2, and k_3 are the quenching rate coefficients of O(^{1}D) by N_2, O_2, and O, respectively, and A_{1D} and A_{2D} are the transition coefficients for 630.0 nm and 636.4 nm emission, respectively. All the values of the parameters and the formulas for the rate coefficients can be found in Chiang et al. (2018).

It was found that the observed enhancement area of the 630.0 nm emissions moved poleward with time. It is known as the midnight brightness wave (MBW) (Herrero and Meriwether 1980; Colerico et al. 1996; Colerico and Mendillo 2002). Previous studies have also shown that these 630.0 nm-enhanced emissions are signs of the effects of the midnight temperature maximum (MTM) (Meriwether et al. 2008; Adachi et al. 2010; Chiang et al. 2018), which is a large-scale neutral temperature anomaly in the low-latitude thermosphere at midnight.

Ground-based all-sky cameras have been widely used for airglow observations, of which MBW is one of the popular topics of study (Colerico et al. 1996; Otsuka et al. 2003; Shiokawa et al. 2006). Ground-based imager observations (Burnside et al. 1977; Chang et al. 2015; Fukushima et al. 2017) are suitable for obtaining long-term observational data for local investigations. On the other hand, satellite imager observations (Mende et al. 1993; Chang et al. 2012; Chiang et al. 2018) are suitable for time-limited but global observations. It is important to investigate MBW on the basis of global distributions of midnight brightness.

Adachi et al. (2010) showed the 630.0 nm nightglow observations around midnight obtained by the Imager of Sprites and Upper Atmospheric Lightning (ISUAL) science payload onboard the FORMOSAT-2 satellite (Chang et al. 2012; Frey et al. 2016). They studied two weeks of image data obtained from the Asian sector, where the tendency of the equatorial nightglow appeared to correspond to the MBW features. Chiang et al. (2013) investigated the long-term behavior of 630.0 nm midnight brightness, also using ISUAL side-viewing image data. They considered a data set that included all the regions covered by ISUAL over a duration of 21 months. They found that enhanced nightglow always appears near the equatorial regions, where significant seasonal variations in intensities were observed for the 630.0 nm emission. Their conclusion was that it is necessary to take into

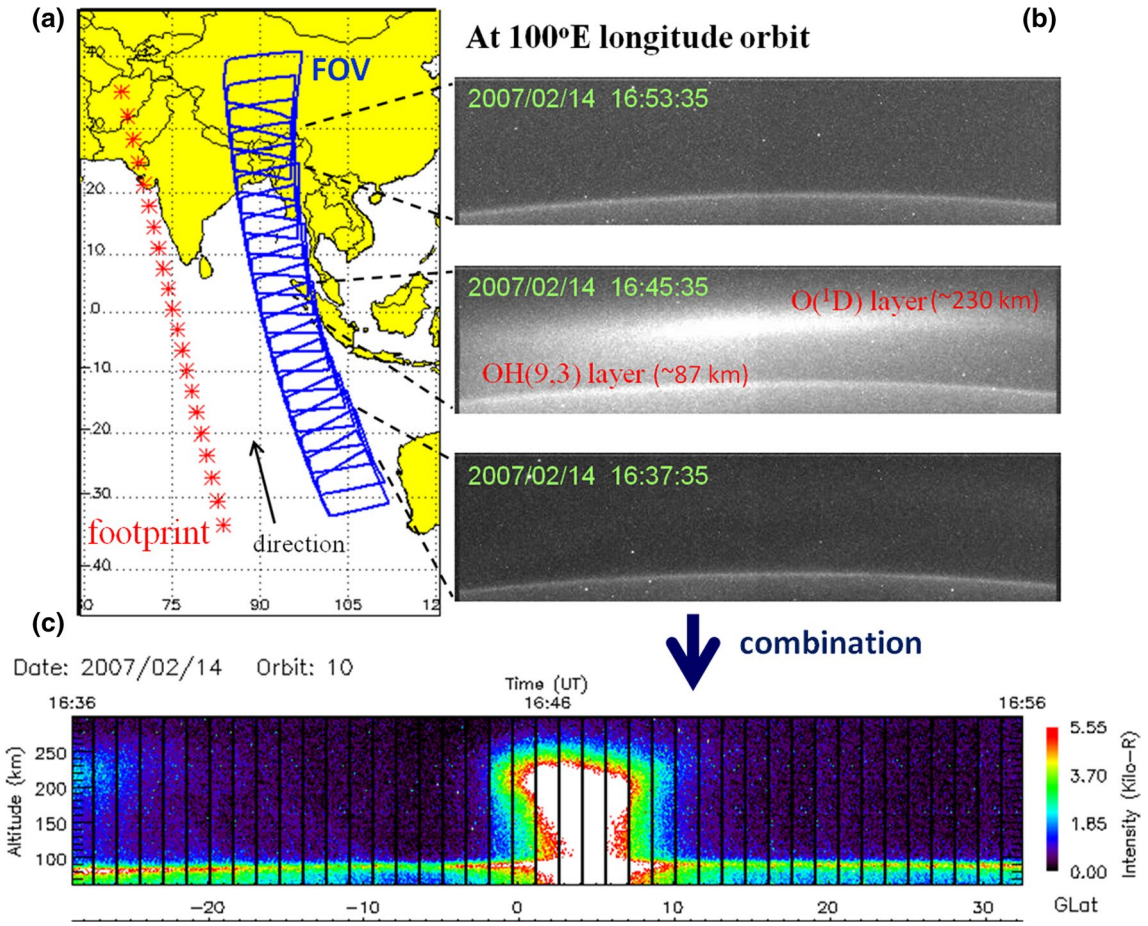

Fig. 1 **a** Ground projection of the satellite tracks (red stars) and the corresponding FOV (blue lines) for a typical observation in an orbit; **b** three typical ISUAL 630.0 nm images taken in the night of 14 Feb., 2007, corresponding to the FOV in **a**; **c** a combined image for the orbit shown in **a**

account the locations and seasons in order to explain the enhanced nightglow mechanism.

However, Chiang et al. (2013) only provided the statistical results on the probabilities of different types of brightness for all orbits. In order to understand the combined effects of locational and seasonal variations, it is necessary to separate the regions according to the relationship between the geographic equator and the geomagnetic equator. Thus, in this paper we report the midnight airglow enhancements for nearly 2 years' observations and show the statistical results corresponding to the different longitudinal regions. As far as we know, this is the first study to provide the global distribution of equatorial midnight brightness.

Instrumentation and observations

The scientific payload ISUAL was placed onboard the FORMOSAT-2 spacecraft, which was launched on May 21, 2004 and decommissioned in August 2016. The FORMOSAT-2 spacecraft moved along a sun-synchronized orbit at 890 km altitude, making 14 revolutions per day. When ISUAL tracked from south to north with its eastward viewing configuration, it observed airglow emissions around local midnight (~2330 LT). The possible observing local time range can be 2330 ± 7 LT throughout the four seasons investigated in this paper. ISUAL can observe airglow emissions on the same orbit for about 20 min, and one orbit covers about 60 degrees of latitude. The Charge Coupled Device (CCD) Imager provided a 20° (horizontal) × 5° (vertical) field of view (FOV) with 516 × 128 (pixel) image resolution.

Figure 1 features an example of one orbital observation. The footprints of the satellite and its FOV are shown in Fig. 1a, and some examples of the raw images are shown in Fig. 1b. Under the normal observation mode, the Imager took a picture every 30 s for 20 min during each orbit. Taking into account the overlap between adjacent snapshots in the ISUAL observations, we were able to integrate dozens of individual images into a wide-field picture for a given orbit. After the necessary calibration

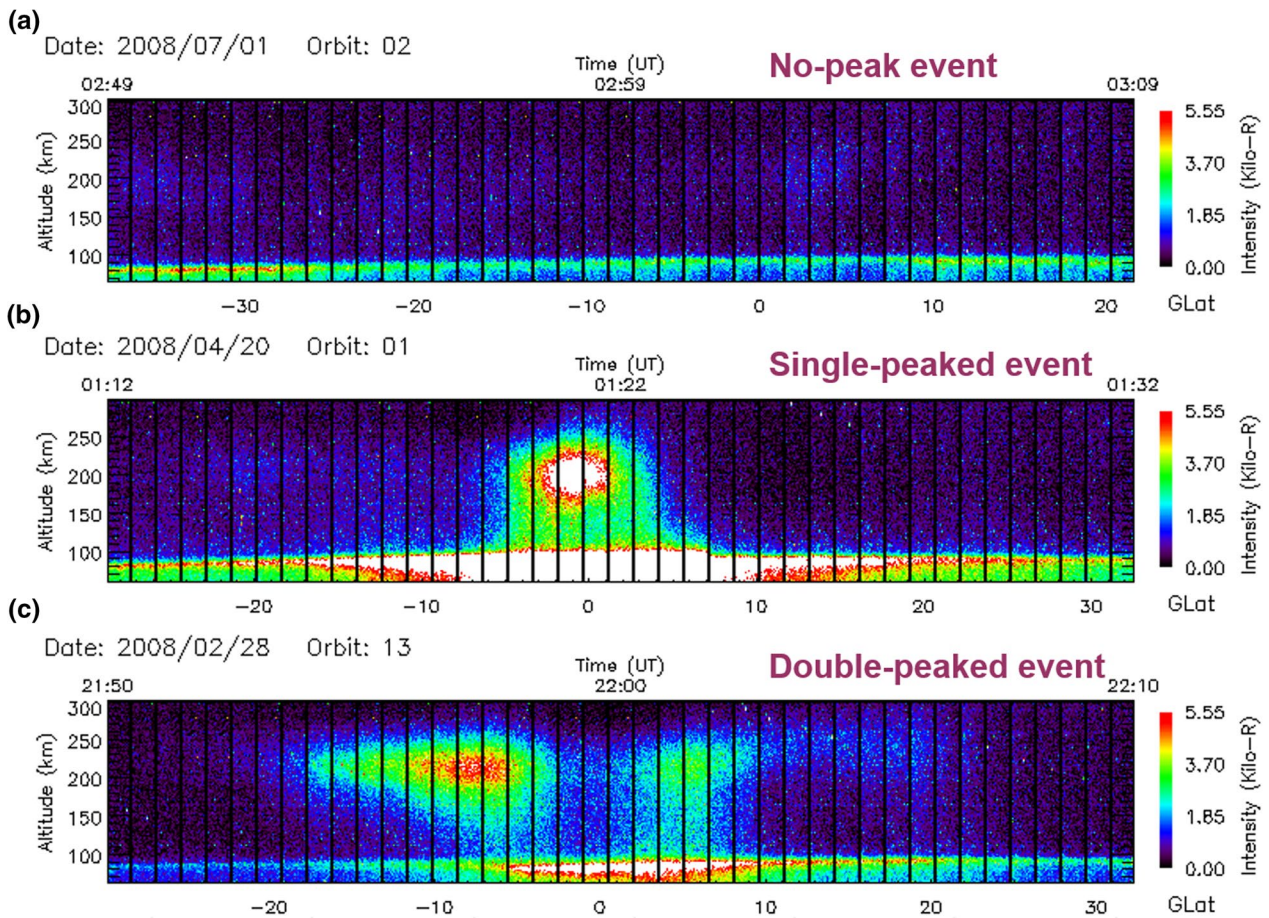

Fig. 2 Three types of equatorial brightness events around midnight observed by ISUAL: **a** a no-peak event; **b** a single-peaked event; **c** a double-peaked event

process (Chen et al. 2012; Chiang et al. 2013), the calibrated and combined latitude-altitudinal wide-range distributions are shown in Fig. 1c. The vertical black lines partition the contribution from each exposure of a given orbit. Chiang et al. (2013) and Tam et al. (2021) both presented the similar combined wide-range image plots and they explained the combined plots in detail. The image shows two different emission layers located at different altitudes. The higher emission layer is due to the OI(^{1}D) airglow emission process, and the lower emission layer is due to the OH(9,3) airglow emission process (Mende et al. 1993). In this paper, we focus on the OI(^{1}D) enhancements at altitudes of approximately 230 km in relation to plasma variations. It is noted that the estimated peak altitude we showed here is lower than the actual peak of volume emission rate because of a side-viewing integration effect (Tam et al. 2021).

Figure 2 shows three types of events based on the ISUAL wide-range observational results. Figure 2a shows an example where there was no-peak enhancement during the period of interest, which is called a no-peak event. Figure 2b shows an example of the enhancement with a single peak near the geographic equator, which is labeled as a single-peaked event. Figure 2c shows an example

(See figure on next page.)

Fig. 3 Global mapping of the brightness locations of all of the orbital observations, grouped by the season: The sequence of the seasons is as follows: **a** Feb.–Apr. 2007, **b** May–Jul. 2007, **c** Aug.–Oct. 2007, **d** Nov. 2007–Jan. 2008, **e** Feb.–Apr. 2008, **f** May–Jul. 2008, and **g** Aug.–Oct. 2008. Single-peaked events are shown as red circles, and double-peaked events are shown as solid blue triangles and green squares. The dotted lines indicate the geomagnetic equator, and the solid lines at 0° latitude correspond to the geographic equator

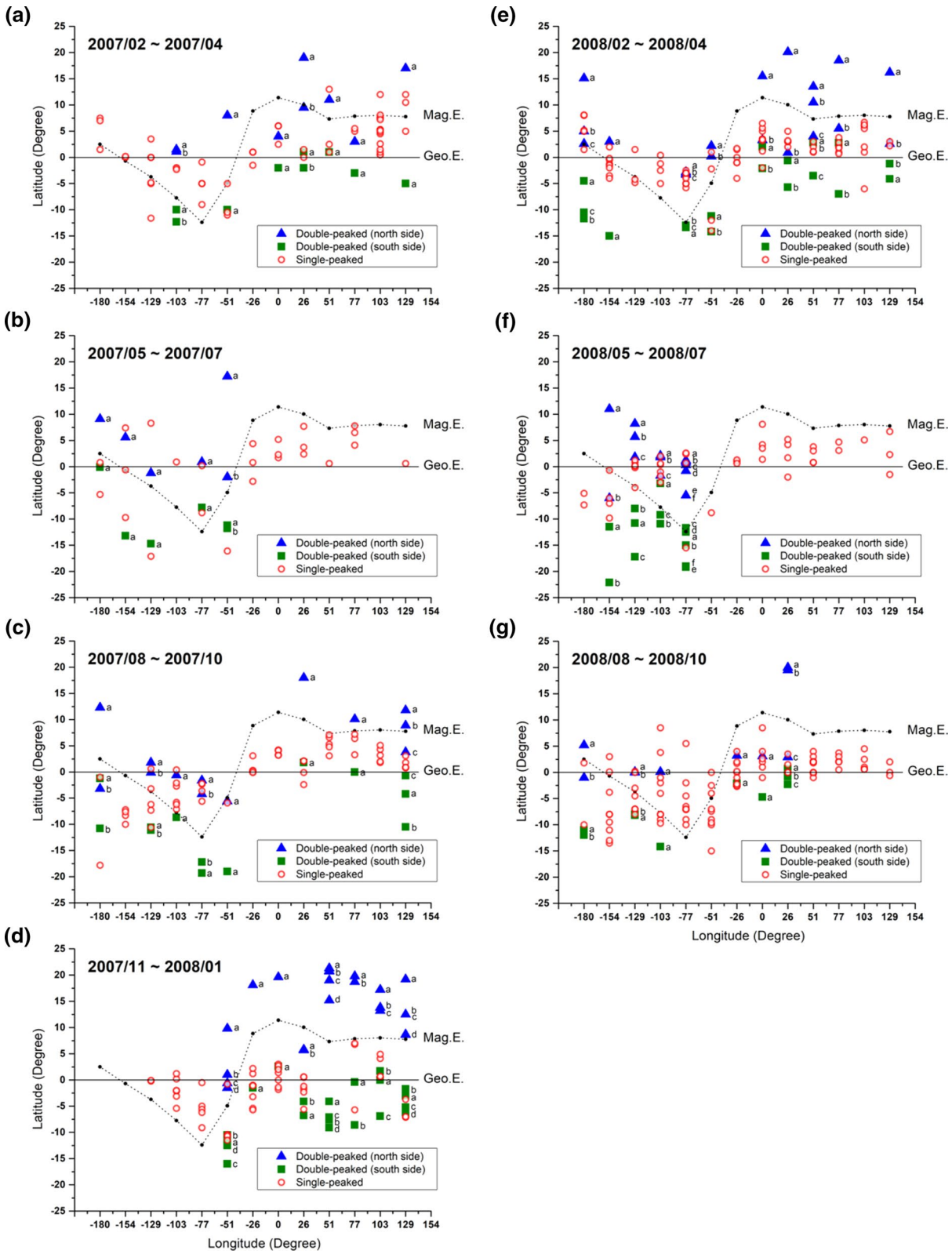

Fig. 3 (See legend on previous page.)

of the enhancement with double peaks, called a double-peaked event.

Observation results

Based on the same criteria as those in previous studies for quiet-time periods (Chiang et al. 2013), we have collected 535 orbital data from the ISUAL nightglow observations between February 2007 and October 2008 for a total of 21 months (7 seasons) for the analysis and statistics in this study. In this study, we considered that when the brightness was above 2 kR (kilo-Rayleigh) and the brightness ranged no less than 5° in latitudes, a brightness event occurred. The criteria we used have also been adopted in the work of Tam et al. (2021). Tam et al. (2021) carried out the retrieval of airglow emission rates for ISUAL images. Before the decommissioning of ISUAL, the only complete airglow observation period was from 2007/01 to 2008/10. Therefore, we are unable to present the complete two-year ISUAL observation results. But we can still get enough information for analysis from the 21-month observational data.

Figure 3 shows the global mapping of the observed brightness locations in each of the 7 seasons. The seasons are shown in sequential order: Fig. 3a for February–April 2007 (single-peaked: 46, double-peaked: 9, and no-peak: 8), Fig. 3b for May–July 2007 (single-peaked: 25, double-peaked: 6, and no-peak: 18), Fig. 3c for August–October 2007 (single-peaked: 47, double-peaked: 13, and no-peak: 10), Fig. 3d for November 2007–January 2008 (single-peaked: 46, double-peaked: 21, and no-peak: 5), Fig. 3e for February–April 2008 (single-peaked: 60, double-peaked: 20, and no-peak: 4), Fig. 3f for May–July 2008 (single-peaked: 42, double-peaked: 14, and no-peak: 32), and Fig. 3g for August–October 2008 (single-peaked: 74, double-peaked: 10, and no-peak: 25). We can find that the no-peaked category cannot show up in this figure. Regarding their distribution in longitude, we can learn about them through the quantity we wrote here with the chapter of statistical analysis later. The red circles denote single-peaked events; the solid blue triangles denote the northern part of double-peaked events, and the green squares denote the southern part of the double-peaked events. In order to enable readers to clearly distinguish the pairing positions of double-peaked events, we add an additional English symbol next to the paired double-peaked events to distinguish them. The dotted lines indicate the geomagnetic equator, and the solid lines at 0° latitude correspond to the geographic equator. Note that the positive sign in the vertical axis represents the north latitude, and the positive sign in the horizontal axis represents the east longitude.

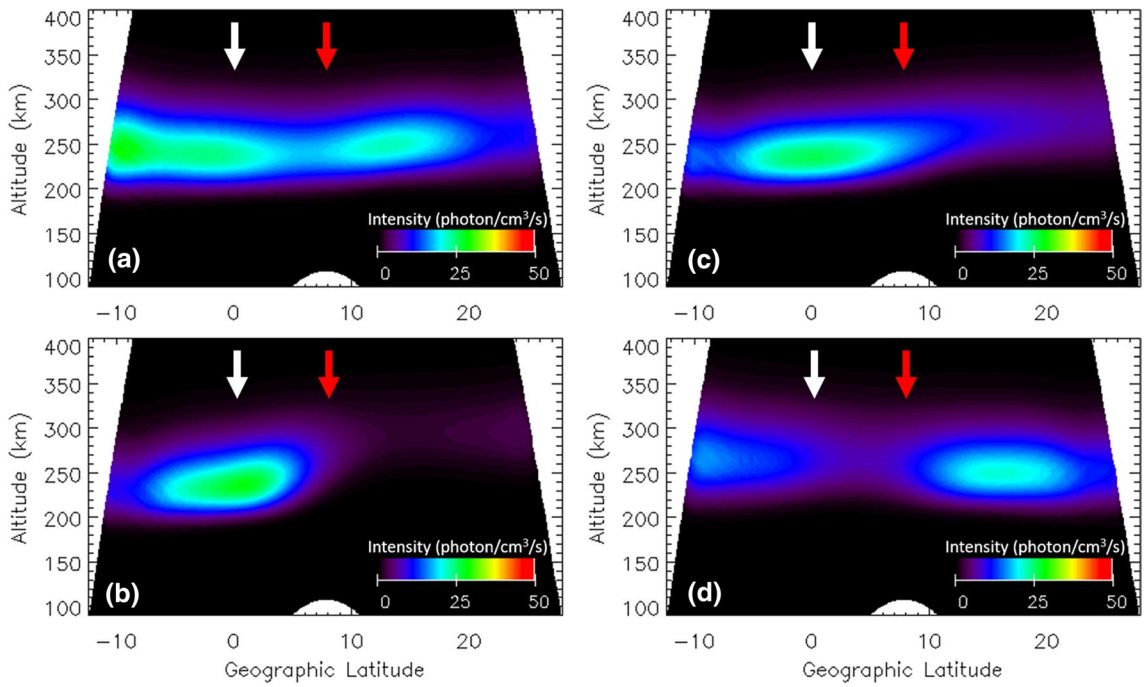

Fig. 4 Simulation results of the 630.0 nm nightglow based on the SAMI-2 model, plotted in the latitude-altitudinal plane at midnight on **a** March 1, 2007, **b** June 1, 2007, **c** September 1, 2007, and **d** December 1, 2007 along the 50°E longitude. The white arrows indicate the geographic equator, and the red arrows indicate the geomagnetic equator

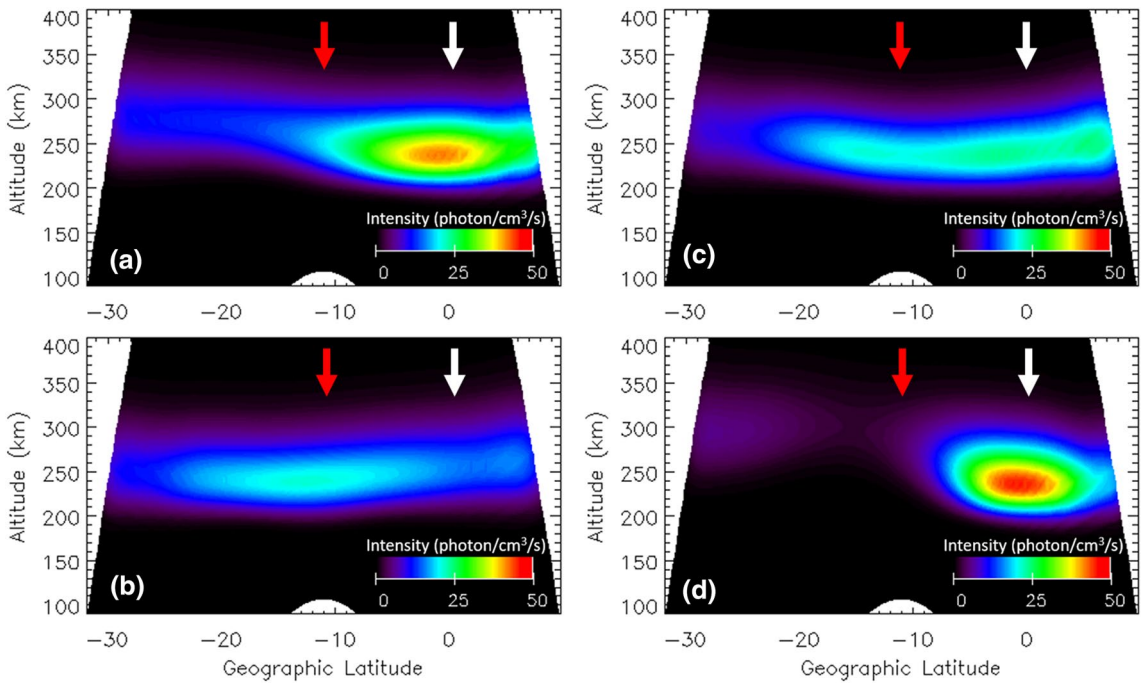

Fig. 5 The same as in Fig. 4, but along the 80° W longitude

According to the global distributions of the brightness locations shown in Fig. 3, overall, the midnight brightness mostly appeared in the vicinity of the geographic equator, especially for the single-peaked events, which mostly occurred between the geographic equator and the geomagnetic equator. The brightness of double-peaked events tended to appear slightly farther away from the geographic equator than that of single-peaked events. For the double-peaked events, we did not find any case during the northern summer in the region where the geomagnetic equator was to the north of the geographic equator. They were also not found during the northern winter in the region where the geomagnetic equator was to the south of the geographic equator.

Simulation results

In this study, we also calculate the volume emission rates of the 630.0 nm nightglow (Eq. 1) based on parameters generated by the SAMI-2 model from the Naval Research Laboratory (Huba et al. 2000), and compare the results with the ISUAL observations. SAMI-2 is a two-dimensional, first-principle model of the low to mid-latitude ionosphere. With latitudes and altitudes as its spatial domain, the model is very suitable for simulations of the latitude-altitudinal airglow distribution, as the results can be readily presented in the same way as the ISUAL observations for comparison. The simulation results of the 630.0 nm nightglow are plotted for the midnights on March 1, June 1, September 1, and December 1, 2007, and are shown in Figs. 4 and 5. The difference between Figs. 4 and 5 is that the results are for different longitudes. Figure 4 shows the results at 50° E longitude, and Fig. 5 shows the results at 80°W longitude. The white arrows indicate the geographic equator, and the red arrows indicate the geomagnetic equator in these figures. The geomagnetic equator is to the north of the geographic equator for the locations in Fig. 4, but to the south of the geographic equator for the locations in Fig. 5.

Single-peaked enhancements appear in northern summer and autumn near the geographic equator at the longitude shown in Fig. 4. In northern spring and winter, there are double-peaked enhancements with one peak on each side of the region sandwiched by the two equators. In contrast, at the longitude shown in Fig. 5, single-peaked enhancements appear in northern spring and winter near the geographic equator, with the more luminous single-peaked brightness occurring in northern winter. As for northern summer and autumn, the enhancement appears fuzzy and extends from the geographic equator to the geomagnetic equatorial region.

In order to further understand whether the SAMI2 simulation can explain the results of ISUAL observations, we compared the simulation results in Fig. 4 with the observation results of 50°E longitude (the fourth orbit from the right) shown in Fig. 3. We also compared the

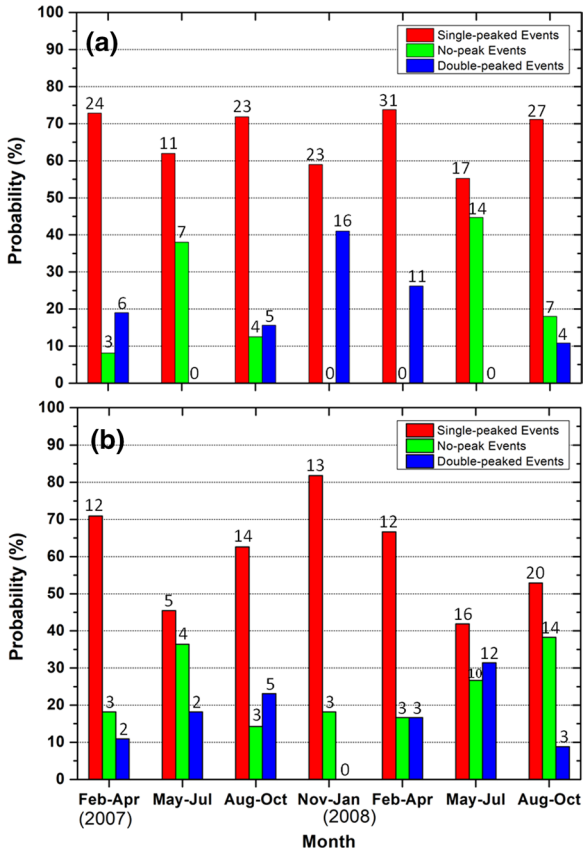

Fig. 6 Combined occurrence rates of the three types of brightness from all the orbits during the 7 seasons: **a** for the region between the 0° and 150° longitudes (Zone-N); **b** for the region between the − 75° and − 15° longitudes (Zone-S). Single-peaked events are in red, double-peaked events are in blue, and no-peak events are in green. The numbers at the top of bar are event numbers

simulation results of Fig. 5 with the observation results of 80°W longitude (the ninth orbit from the right) as shown in Fig. 3.

First, we compare the two results at 50°E longitude. Figure 3a shows that the locations of brightness in this orbit were distributed from the geographic equator to the geomagnetic equator and beyond. Figure 4a also shows a wider area of brightness by comparison. Figure 3b, c shows that the locations of brightness were distributed between the geographic equator and the geomagnetic equator. Correspondingly, Fig. 4b, c also shows that the centers of the brightness areas were between the geographic equator and the geomagnetic equator. Finally, Fig. 3d shows that the double-peaked brightness was located on the two sides of the region sandwiched by the two equators. It corresponded to the simulation result of Fig. 4d showing the same characteristics.

Next, we compare the two results at 80°W longitude. Figure 3a shows that the locations of brightness in this orbit were distributed between the geographic equator and the geomagnetic equator. Correspondingly, Fig. 5a shows that the center of the brightness area was mainly between the geographic equator and the geomagnetic equator, but tended to be close to the geographic equator. Figure 3b shows that the locations of brightness were mainly distributed between the geographic equator and the geomagnetic equator, and one event of double-peaked brightness started to appear in this season. In Fig. 5b, the brightness area was relatively less concentrated than other single-peaked events, covering a wider area around the geomagnetic equator. Figure 3c shows that the double-peaked brightness started to cross the geomagnetic equator. Correspondingly, Fig. 5c also shows that the brightness area appeared expansive and its area exceeded the geomagnetic equator. Finally, Fig. 3d presents the same distribution as Fig. 3a, and the brightness was located between the geographic equator and the geomagnetic equator. This also corresponded to the simulation results shown in Fig. 5d.

Statistical analyses from observations

In order to understand the possible mechanisms for the occurrence of the three types of equatorial midnight brightness, we examine their occurrence rates in every 3-month period. These occurrence rates are shown in Fig. 6 with bar plots, where single-peaked events are shown in red, double-peaked events in blue, and no-peak events in green. The numbers at the top of bar are event numbers. In order to understand the influence of geomagnetic conditions, the statistical analyses are separated into two zones: Fig. 6a shows the results for the region between the 0° and 150° longitudes (named Zone-N), and Fig. 6b features the region with longitudes ranging from − 75° to − 130° (named Zone-S). Before the decommissioning of ISUAL, the only complete airglow observation period was from 2007/01 to 2008/10. Therefore, the complete 2-year ISUAL observation results are not available. So we present the 21-month observational data in this study. From the results in Fig. 6, we found that the occurrence of the three types of events has strong periodicity. First, it is found that no-peak events (green bar) frequently occur during the northern summer (May–July) in both zones. Second, double-peaked events (blue bar) tend to appear during the northern winter in Zone-N but during the northern summer in Zone-S. Third, single-peaked events (red bar) exhibit a semi-annual cycle in Zone-N but tend toward an annual cycle in Zone-S. This is the first study that reports the differences between Zone-N and Zone-S in midnight brightness.

Discussion

Colerico et al. (1996) reported that the typical initial period of occurrence of MBW is between 23:00 and 01:00 LT, and then it begins to spread toward the polar regions, forming the V-shaped MBW in a plot of latitude vs. LT. Since the ISUAL observation time in our study is close to midnight, such a local time falls within the initial generation window of the MBW. Therefore, it can explain why most of the events we observed, regardless of region or season, are mostly single peaked in brightness. The occurrence rates of single-peaked events are the highest in every combination of seasons and zones, as shown in Fig. 6.

Chiang et al. (2013) has found the locations of single-peaked brightness tend to appear between the geographic and geomagnetic equators. This tendency is also clearly presented in the global mapping in this study, as shown in Fig. 3. In different seasons and longitudinal regions, the single-peaked brightness was mainly formed between the geographic equator and the geomagnetic equator. We speculated that the latitudinal locations of brightness are geomagnetic field dependent near the equatorial regions. Based on the volume emission rate of the 630.0 nm nightglow in Eq. (1), O^+ is the key variable factor for the emission and it can be controlled by the field lines. But the new observational results still need to be examined more specifically as a topic by more research in the future.

According to the studies by Meriwether et al. (2008) and Adachi et al. (2010), some double-peaked events represent a cross section of the two branches of the V-shaped MBW. In this study, regarding the occurrence rates of double-peaked events in different seasons, we believe that the summer-to-winter (trans-equatorial) neutral wind (Harper 1973) plays an important role. Neutral wind will not only cause the positions of double-peaked events to be changed but it may also change the amount of brightness. Rishbeth (1972) and Torr and Torr (1973) reported that the winter anomaly was due to a summer-to-winter neutral wind that caused the F2-layer peak electron density (NmF2) to be higher in the winter than it was in the summer hemisphere. The winter anomaly also contributes to the observed results in our study.

Chiang et al. (2018) has successfully proved that the influence of neutral wind effect on 630.0 nm nightglow is much greater than that caused by temperature changes based on their simulation and calculation results. Furthermore, they also used simulation data to prove that the neutral wind has an absolute influence on the final position of the plasma clumps. Based on the nightglow simulation results in this study, we find that nightglow brightness does tend to appear near the geographic equator (white arrow) for most seasons, as shown in Figs. 4a–c, 5a, c, d. In addition, the enhancement would extend to the geomagnetic equator or shift to the other side of the geomagnetic equator in the winter hemisphere, as shown in Figs. 4d, 5b. The appearance of the brightness locations is consistent with the results of seasonal plasma distribution presented by Chiang et al. (2018).

From the global mapping of brightness shown in Fig. 3, we can confirm that there were no double-peaked events for the following two situations, northern summer in Zone-N (Fig. 3b, f), and northern winter in Zone-S (Fig. 3d). However, based on the development of two branches of the V-shaped MBW, the double-peaked events should be observed in a certain chance in any seasons and zones. The most likely reason is that the neutral wind blows from the northern hemisphere to the southern hemisphere at northern summer (Fig. 3b, f), the brightness is not easy to form on the north side of the geomagnetic equator in Zone-N. In contrast, the neutral wind blows from the southern hemisphere to the northern hemisphere at northern winter (Fig. 3d), the brightness is also not easily formed on the south side of the geomagnetic equator in Zone-S. Overall, the summer-to-winter neutral winds could hinder the generation of double-peaked events in the above two situations. Regarding the dynamic mechanism of the neutral wind on the position of the brightness, we have a detailed explanation in the Appendix.

If we focus on the double-peaked events in Fig. 3 (only Zone-N and Zone-S are calculated), we also found interesting results produced by the neutral wind effect. There is about 61.5% chance that one of the brightness of a double-peaked event could cross to the other side of the geomagnetic equator during the Equinox periods. But during the Solstice periods, this probability increases to 82.8%. This means that the effect of neutral wind not only inhibits the generation of double-peaked events but also makes it easier for the one of the brightness of the previously existing double-peaked events to cross the geomagnetic equator. It all depends on the direction of the neutral wind and the movement of the MBW, as well as the relative position of the geomagnetic equator.

Ideally, the double-peaked event formed by the V-shaped MBW should be symmetrical to the geographic equator. However, Herrero and Spencer (1982) reported that the initial position of MTM brightness may appear at any low latitudes in the summer hemisphere. As a result, most of the V-shaped MBW development may not be symmetrical to the geographic equator. Moreover, driven by the neutral wind, the plasma may move up or down along the field line away from the emission height of the airglow. Therefore, when we want to understand the generation mechanism of nightglow brightness, we not only need to know the number and location of brightness but

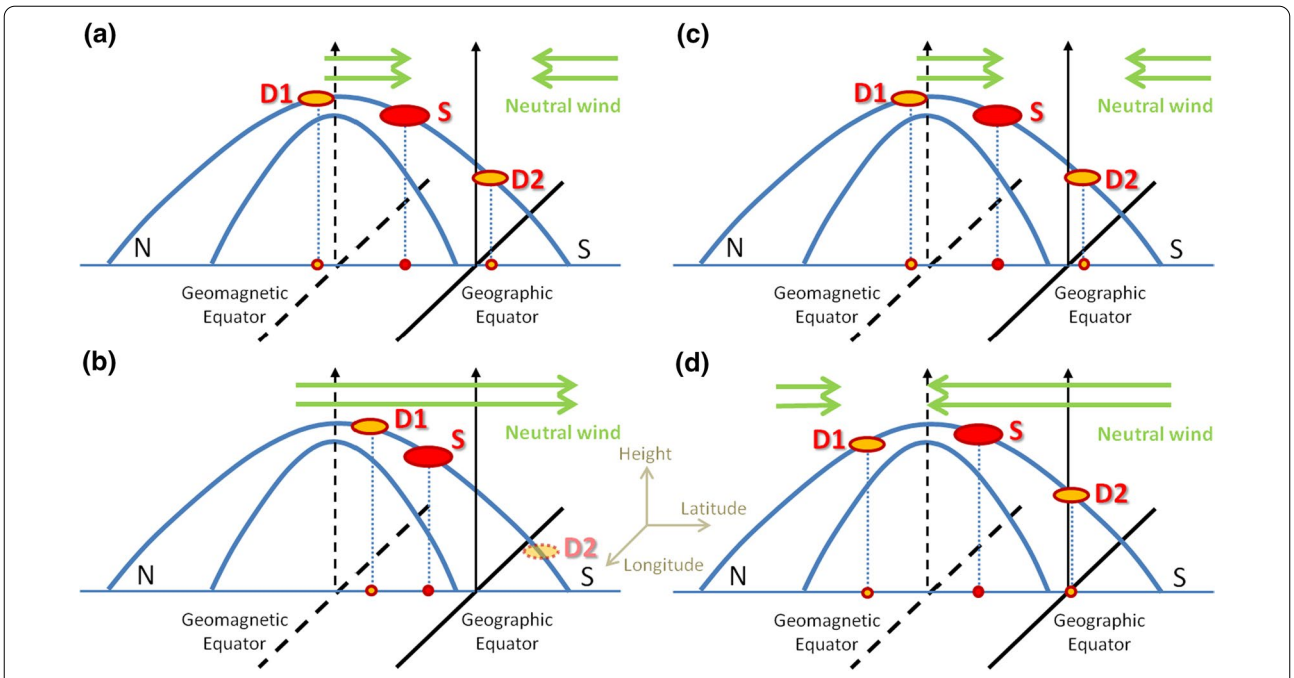

Fig. 7 Schematic diagram of single-peaked and double-peaked brightness behavior with neutral wind at Zone-N in the northern **a** spring, **b** summer, **c** autumn, and **d** winter season

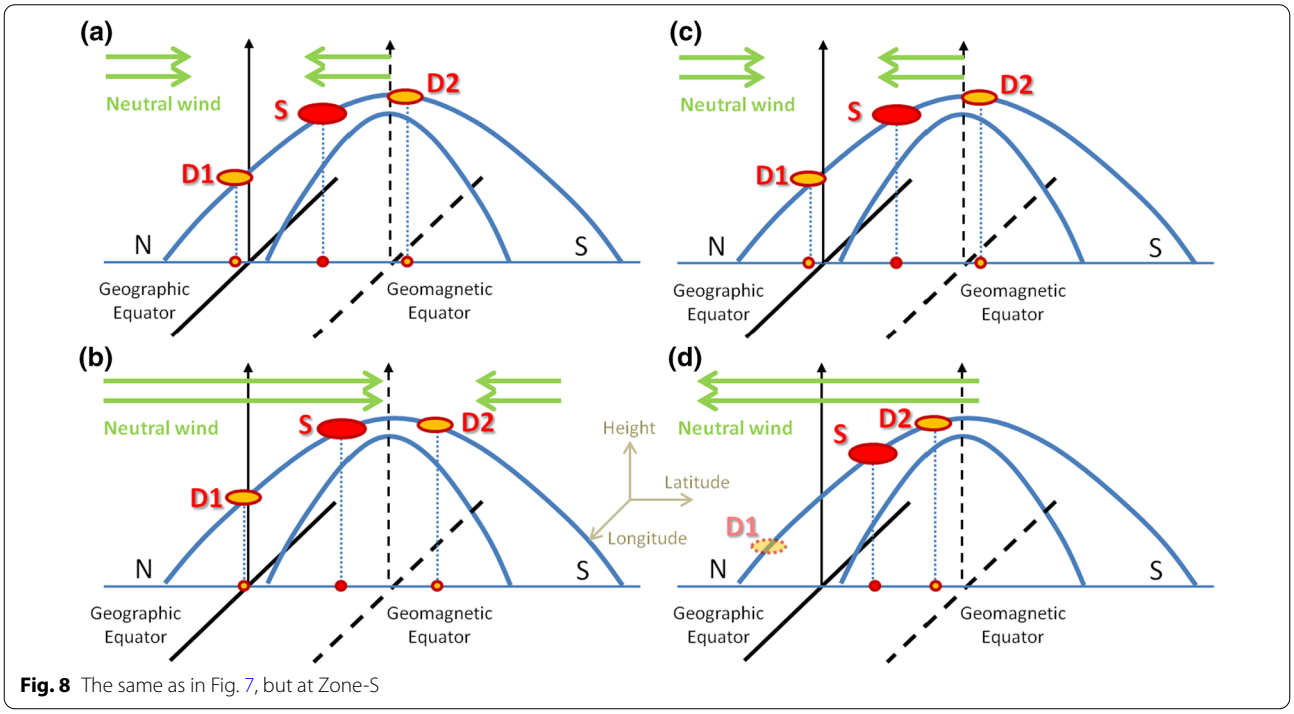

Fig. 8 The same as in Fig. 7, but at Zone-S

also need to make a correct explanation in accordance with the seasonal changes in statistics.

Another point to note is that, sometimes the equatorial ionospheric anomaly (EIA) crest is intensified by pre-reversal enhancement (PRE) after sunset. This is similar to a double-peaked event, which causes two peaks to appear on both sides of the geomagnetic equator. However, many studies in the past have shown that

the strengthening effect caused by PRE only lasts 1 to 2 h (Balan et al. 2018; Huang 2018; Ebenezer et al. 2021). In other words, the post-sunset EIA crests disappear after about 21 LT. This is far from the observation time of ISUAL. Therefore, we believe that the double-peaked events observed by ISUAL were unlikely a consequence of EIA.

Ionospheric annual anomalies have been thoroughly investigated in the literature. Su et al. (1998) found that the electron densities within the latitude range $\pm 25°$ are higher at the December solstice than at the June solstice. Titheridge and Buonsanto (1983) measured at conjugate sites at $\pm 20°$ latitude and also found the lowest total electron content (TEC) occurs in the June solstice. These early findings suggested that brightness enhancement would be less likely to occur in the northern summer. They could therefore explain the tendency of the occurrence rate of no-peak events in our observations, which on average feature relatively highest probability in the May–July season regardless of the zone (Zone-N or Zone-S), as shown in Fig. 6.

Overall, there are some very interesting features in Zone-N and Zone-S for the three types of events shown in Fig. 6. First, single-peaked events exhibited a semi-annual cycle in Zone-N and an annual cycle in Zone-S. Second, double-peaked events exhibited an annual cycle in Zone-N and Zone-S, where the maximum number of events occurred in the northern winter and southern winter, respectively. No-peak events also exhibited an annual cycle in Zone-N and Zone-S, where the maximum number of events both occurred in the northern summer.

It is particularly worth mentioning that single-peaked events exhibit a semi-annual cycle in Zone-N and an annual cycle in Zone-S. We assumed that the probabilities of single-peaked brightness generated by the MTM effect are the same in all seasons or regions. As explained above, the probability of no-peak events was likely to increase in the May–Jul. season due to the decrease in electron density. The double-peaked events tended to appear in the Nov.-Jan. season at Zone-N as well as the May–Jul. season at Zone-S because of the summer-to-winter wind. Therefore, because of the increase of no-peak and double-peaked events, the probability of occurrence of the single-peaked events was reduced in the specific seasons mentioned above. As shown in Fig. 6, the final result of single-peaked event shows a semi-annual cycle at Zone-N and an annual cycle at Zone-S.

In general, based on our observations and simulation studies, the MTM effect produces single-peaked brightness at midnight between the geographic equator and geomagnetic equator. Then, the brightness slowly moves toward the two poles due to a pressure bulge (Colerico and Mendillo 2002; Niranjan et al. 2006; Fang et al. 2016), developing into a double-peaked event at the time. However, with the different geomagnetic field conditions at different locations, coupled with the summer-to-winter wind generated by seasonal effects, the plasma may have the opportunity to be blown to the other hemisphere along the magnetic field lines. Therefore, the location of the brightness can be changed, and even its emission rate can be changed.

In order to let readers better understand the influence of neutral wind on brightness, we made the schematic diagrams shown in Figs. 7 and 8. Figures 7 and 8, respectively, show the changes in Zone-N and Zone-S in different seasons. The schematic diagrams show the same three-dimensional architecture. The vertical axis represents the height direction, the horizontal axis represents the latitude, and the axis perpendicular to the height-latitude plane represents the longitude. The black solid line represents the geographic equator, the black dashed line represents the geomagnetic equator, and the blue solid line represents the structure of the magnetic field lines. The red blocks (named S) in the figures represent the single-peaked event and their projection points are also marked on the latitude axis. The yellow blocks (named D1 and D2) represent the double-peaked event and their projection points are also marked on the axis of latitude. The green solid arrows represent the directions of the neutral wind.

In Fig. 7a, c, the neutral winds in these two seasons are mostly symmetric to the geographic equator. The two wind fields blow in opposite directions, reducing the intensity of the overall wind. So whether it is a single-peaked event or a double-peaked event, they tend to remain in the original state when they are observed. In Fig. 7b, the summer-to-winter neutral wind blows from the northern hemisphere to the southern hemisphere. The D1 brightness is not easy to move across to the north side of the geomagnetic equator. The plasma clump of D2 brightness tends to be taken to a lower height and get out of the emission layer. So when it is observed, it still appears in a single-peaked state. In Fig. 7d, the summer-to-winter neutral wind is blowing from the southern hemisphere to the northern hemisphere. The D1 brightness is more easily maintained on the north side of the geomagnetic equator. The D2 brightness is at most slightly moved. Therefore, D1 and D2 maintain the double-peaked state. This also means that double-peaked events are more likely to be found in this season.

Figure 8a, c shows the same wind field condition as Fig. 7a, c. The two wind fields blow in opposite directions, and therefore, both the single-peaked event and the double-peaked event tend to maintain the original states. The effect of Fig. 8b is similar to that of Fig. 7d. Double-peaked events are more likely to be found in the

season. Finally, the effect of Fig. 8d is similar to that of Fig. 7b. Brightness is not easy to move across to the other side of the geomagnetic equator, and therefore, only single-peaked events appear.

Conclusion

In this study, we use ISUAL data to complete observational statistics over a nearly two-year period. The physical mechanism of midnight brightness is discussed and verified with the SAMI-2 model. The observation and simulation results are consistent. We believe this is the first time a complete statistical research report is presented without any bias in terms of observation. The key contributions of this study are as follows:

1. Single-peaked brightness is observed most easily near midnight, and it is mostly occurred between the geographic equator and the geomagnetic equator.
2. If MTMs occur earlier, it is possible to see double-peaked brightness in the ISUAL observations. However, due to the influence of summer-to-winter neutral wind, the secondary brightness cannot occur in the Zone-N area during the northern summer. Similarly, the secondary brightness cannot occur during the northern winter period in Zone-S.
3. The rate of occurrence of no-peak events is relatively high in the period close to May–July. This may be due to the effects of ionospheric annual anomalies.
4. With combination of the above factors, single-peaked events exhibit a semi-annual cycle in Zone-N and an annual cycle in Zone-S. Double-peaked events exhibit annual cycles in Zone-N and Zone-S, where the maximum number of events occurs in the northern winter and southern winter, respectively. No-peak events also exhibit an annual cycle in both Zone-N and Zone-S, where the maximum number of events occurs in northern summer in both zones.

Supplementary Information

The online version contains supplementary material available at https://doi.org/10.1186/s40623-022-01596-4.

Additional file 1: Figure S1. Schematic diagram of neutral wind effects acting on the ionosphere plasma. The blue arrows show the preset neutral wind direction, and the red blocks are the preset initial positions of plasma clump (Chiang 2020). **Figure S2.** The changes of plasma position along the field line (altitudes and geographic latitudes) with time along the magnetic field line (red curve in Fig. S1). Panels **a** and **b** for 100 m/s wind speed; **c** and **d** for 200 m/s wind speed; **e** and **f** for 300 m/s wind speed.

Acknowledgements
The authors acknowledge the Taiwan National Space Organization (NSPO) for providing ISUAL data.

Authors' contributions
CYC performed the statistical analysis and drafted the part of manuscript. TFC analyzed the data and also drafted the part of manuscript. SWYT participated in the discussion of the analysis method and results. All the authors read and approved the final manuscript.

Funding
The work of Chih-Yu Chiang is supported by Taiwan Ministry of Science and Technology Grants MOST 109-2112-M-006-007 and MOST 110-2112-M-006-022. The work by Tzu-Fang Chang is supported by Taiwan Ministry of Science and Technology Grants MOST 109-2635-M-006-001 and MOST 110-2111-M-006-003.

Availability of data and materials
The ISUAL data used in this study are publicly available at https://cdaweb.gsfc.nasa.gov/pub/data/formosat-rocsat/formosat-2/isual/.

Declarations

Competing interests
The authors declare that they have no conflict of interest.

Received: 11 August 2021 Accepted: 21 February 2022
Published online: 04 March 2022

References

Adachi T, Yamaoka M, Yamamoto M, Otsuka Y, Liu H, Hsiao C-C, Chen AB, Hsu R-R (2010) Midnight latitude-altitude distribution of 630-nm airglow in the Asian sector measured with FORMOSAT-2/ISUAL, *J*. Res, Geophys. https://doi.org/10.1029/2009JA015147

Balan N, Liu LB, Le HJ (2018) A brief review of equatorial ionization anomaly and ionospheric irregularities. Earth Planet Phys 2(4):257–275. https://doi.org/10.26464/epp2018025

Burnside RG, Meriwether JW, Torr MR (1977) Contamination of ground-based measurements of OI (6300 Å) and NI (5200 Å) airglow by OH emissions. Planet Space Sci 25:985–988

Chang TF, Cheng CZ (2015) Relationship between wave-like auroral arcs and Pi2 disturbances in plasma sheet prior to substorm onset. Earth Planets Space 67:168. https://doi.org/10.1186/s40623-015-0334-8

Chang TF, Cheng CZ, Chiang CY, Chen AB (2012) Behavior of substorm auroral arcs and Pi2 waves: implication for the kinetic ballooning instability. Ann Geophys 30:911–926. https://doi.org/10.5194/angeo-30-911-2012

Chen AB, Wu YJ, Chiang CY, Huang YC, Kuo CL, Su HT, Hsu RR, Mende SB, Frey HU, Harris SE, Takahashi Y, Lee LC (2012) Sensitivity degradation of ISUAL instruments and its impact on observations. Terr Atmos Ocean Sci 23:71–83. https://doi.org/10.3319/TAO.2011.06.20.01(AA)

Chiang CY, Chang TF, Tam SW-Y, Huang TY, Chen AB-C, Su HT, Hsu RR (2013) Global observations of the 630-nm nightglow and patterns of brightness measured by ISUAL. Terr Atmos Ocean Sci 24:283–293. https://doi.org/10.3319/TAO.2012.12.13.01(SEC)

Chiang CY, Tam SWY, Chang TF (2018) Variations of the 630.0 nm airglow emission with meridional neutral wind and neutral temperature around midnight. Ann Geophys 36:1471–1481. https://doi.org/10.5194/angeo-36-1471-2018

Colerico MJ, Mendillo M (2002) The current state of investigations regarding the thermospheric midnight temperature maximum (MTM). J Atmos Sol Terr Phys 64:1361–1369

Colerico M, Mendillo M, Nottingham D, Baumgardner J, Meriwether J, Mirick J, Reinisch BW, Scali JL, Fesen CG, Biondi MA (1996) Coordinated measurements of F region dynamic related to the thermospheric midnight temperature maximum. J Geophys Res 101:26783–26793. https://doi.org/10.1029/96JA02337

Ebenezer A-Y, Fagundes PR, Tardelli A, Pillat VG, Pignalberi A, Kavutarapu V, Pezzopane M, Vieira F (2021) Ground and satellite-based observations of ionospheric plasma bubbles and blobs at 5.65° latitude in the Brazilian sector. Adv Sp Res 67:2416–2438. https://doi.org/10.1016/j.asr.2021.01.034

Fang T-W, Akmaev RA, Stoneback RA, Fuller-Rowell T, Wang H, Wu F (2016) Impact of midnight thermosphere dynamics on the equatorial ionospheric vertical drifts. J Geophys Res Space Physics 121:4858–4868. https://doi.org/10.1002/2015JA022282
Frey HU et al (2016) The Imager for Sprites and Upper Atmospheric Lightning (ISUAL). J Geophys Res 121:8134–8145. https://doi.org/10.1002/2016JA022616
Fukushima D, Shiokawa K, Otsuka Y et al (2017) Geomagnetically conjugate observations of ionospheric and thermospheric variations accompanied by a midnight brightness wave at low latitudes. Earth Planets Space 69:112. https://doi.org/10.1186/s40623-017-0698-z
Harper RM (1973) Nighttime meridional neutral winds near 350 km at low to mid-latitudes. J Atmos Terr Phys 35:2023–2034. https://doi.org/10.1016/0021-9169(73)90116-5
Herrero FA, Meriwether JW Jr (1980) 6300 airglow meridional intensity gradients. J Geophys Res 85:4191. https://doi.org/10.1029/JA085iA08p04191
Herrero FA, Spencer NW (1982) On the horizontal distribution of the equatorial thermospheric midnight temperature maximum and its seasonal variation. Geophys Res Lett 9:1179–1182. https://doi.org/10.1029/GL009i010p01179
Huang CS (2018) Effects of the postsunset vertical plasma drift on the generation of equatorial spread F. Prog Earth Planet Sci 5:3. https://doi.org/10.1186/s40645-017-0155-4
Huba JD, Joyce G, Fedder JA (2000) Sami2 is another model of the ionosphere (SAMI2): A new low-latitude ionosphere model. J Geophys Res 105:23035–23053. https://doi.org/10.1029/2000JA000035
Mende SB, Swenson GR, Geller SP (1993) Limb view spectrum of the Earth's airglow. J Geophys Res 98(A11):19117–19125
Meriwether J, Faivre M, Fesen C, Sherwood P, Veliz O (2008) New results on equatorial thermospheric winds and the midnight temperature maximum. Ann Geophys 26:447–466. https://doi.org/10.5194/angeo-26-447-2008
Niranjan K, Brahmanandam PS, Srivani B (2006) Signatures of equatorial midnight temperature maximum as observed from in situ and ground-based ionospheric measurements in the Indian sector. J Geophys Res 111:A07309. https://doi.org/10.1029/2005JA011386
Otsuka Y, Kadota T, Shiokawa K, Ogawa T, Kawamura S, Fukao S, Zhang S-R (2003) Optical and radio measurements of a 630-nm airglow enhancement over Japan on 9 September 1999. J Geophys Res 108(A6):1252. https://doi.org/10.1029/2002JA009594
Rishbeth H (1972) Thermospheric winds and the F-region – A review. J Atmos Terr Phys 34:1. https://doi.org/10.1016/0021-9169(72)90003-7
Shiokawa K, Otsuka Y, Ogawa T (2006) Quasiperiodic southward moving waves in 630-nm airglow images in the equatorial thermosphere. J Geophys Res 111:A06301. https://doi.org/10.1029/2005JA011406
Sobral JHA, Takahashi H, Abdu MA, Muralikrishna P, Sahai Y, Zamlutti CJ, de Paula ER, Batista PP (1993) Determination of the quenching rate of the O(^{1}D) by O(^{3}D) from rocket-borne optical (630 nm) and electron density data. J Geophys Res 98:7791–7798. https://doi.org/10.1029/92JA01839
Su YZ, Bailey GJ, Oyama K-I (1998) Annual and seasonal variations in the low-latitude topside ionosphere. Ann Geophys 16:974–985. https://doi.org/10.1007/s00585-998-0974-0
Tam SWY, Chiang CY, Huang KC, Chang TF (2021) Retrieval of airglow emission rates in analytical form for limb-viewing satellite observations at low latitudes. J Geophys Res Space Physics. https://doi.org/10.1029/2021JA029490
Titheridge JE, Buonsanto MJ (1983) Annual variations in the electron content and height of the F layer in the northern and southern hemispheres, related to neutral composition. J Atmos Terr Phys 45:683–696
Torr MR, Torr DG (1973) The seasonal behaviour of the F2-layer of the ionosphere. J Atmos Terr Phys 35:2237. https://doi.org/10.1016/0021-9169(73)90140-2

Publisher's Note